Bio-Design and Manufacturing (2025) 8:930–947
https://doi.org/10.1631/bdm.2500091

RESEARCH ARTICLE

# Multilayered microfluidic platform for three-dimensional vascularized organ-on-a-chip applications

Chenyang Zhou[1] · Zhangjie Li[1] · Jiaqi Xu[1] · Dingyuan Yu[1] · Lian Xuan[2] · Xiaolin Wang[1,2,3]

Received: 4 March 2025 / Accepted: 16 June 2025 / Published online: 14 November 2025


## Abstract

The vascular network is integral to the developmental and metabolic processes of various tissues and functions as a systemic circulatory system that also interconnects organs throughout the body. In this study, we describe a multilayered microfluidic organ-on-a-chip platform designed for reproducing various three-dimensional (3D) vascularized microtissue models for biological applications. This platform utilizes a porous membrane as a physical barrier and leverages capillary action for hydrogel self-filling. Its high flow resistance mitigates the risk of gel bursting into the medium channels and facilitates the delivery of substances to generate a wide range of interstitial flow and biochemical factor concentration gradients. This study demonstrated that this platform can be used to accurately replicate 3D microenvironments for vasculogenesis, angiogenesis, and vascularized tumor modeling. We also investigated the critical role of multiple microenvironmental regulations in vascular formation on a chip. Moreover, we reproduced the process of tumor angiogenesis, including primary solid tumor features and the inhibitory effects of antitumor drugs on tumor growth and tumor vasculature before and after angiogenesis. Hence, our multilayered microfluidic platform is valuable for exploring multiple vascular mechanisms and constructing specific microtissues that closely mimic in vivo physiological conditions, providing new strategies for cancer research. Furthermore, the multilayered configuration improves design flexibility and scalability, providing the potential for a multi-organ interconnected platform for high-throughput drug screening.

## Graphical abstract

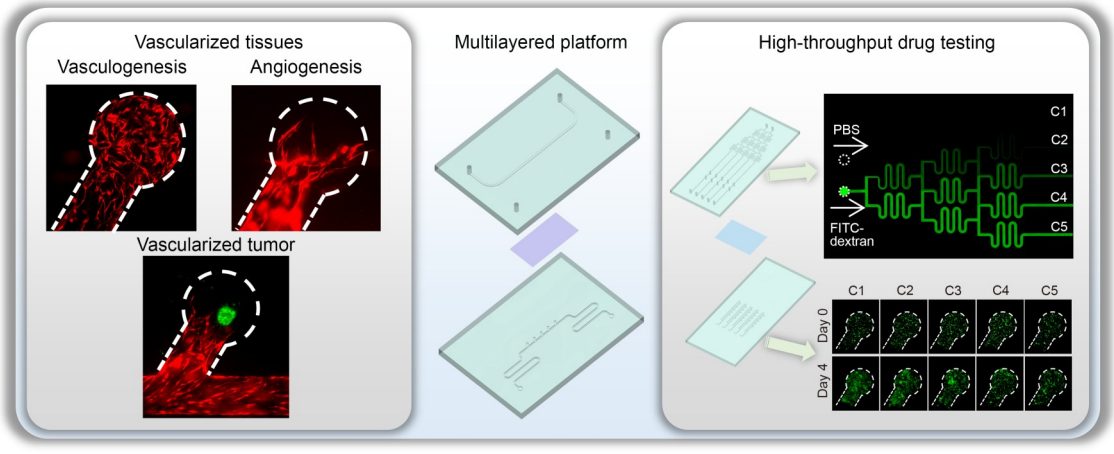


**Keywords** Microfluidics · Multilayered · Organ-on-a-chip · Vascularization

✉ Xiaolin Wang
xlwang83@sjtu.edu.cn

[1] Department of Micro/Nano Electronics, School of Electronic Information and Electrical Engineering, Shanghai Jiao Tong University, Shanghai 200240, China

[2] Institute of Medical Robotics, Shanghai Jiao Tong University, Shanghai 200240, China

[3] National Key Laboratory of Advanced Micro and Nano Manufacture Technology, Shanghai Jiao Tong University, Shanghai 200240, China

## 1 Introduction

The vascular network, integral to systemic circulation, has garnered significant interest due to its multifaceted roles. In addition to facilitating the transport of nutrients across various tissues and maintaining normal metabolic and physiological functions, the vasculature is crucial in tissue repair and regeneration [1], as well as in constructing precise immunoregulatory networks [2]. In the complex tumor microenvironment (TME), vascular formation is a key driver of tumor growth and metastasis, making it a focal point in tumor therapy research. Recent advances in antiangiogenic therapy have demonstrated that pharmacological inhibition of angiogenesis signaling pathways effectively suppresses tumor vascularization, ultimately limiting cancer progression [3, 4]. Furthermore, the combination of antiangiogenic drugs with other therapeutic agents has become an important strategy in the field of targeted tumor therapy [5, 6]. The complex structural properties of the vascular network significantly limit the efficiency of drug penetration in solid tumors. In particular, the physical barrier formed by tight junctions between endothelial cells (ECs) and the dense extracellular matrix (ECM) of the basement membrane impedes drug delivery to the deeper regions of the tumor [7, 8]. Consequently, comprehensive studies on the interaction between vascular properties and drug delivery mechanisms are essential. Such studies not only aid in optimizing existing drug delivery systems to improve drug targeting and bioavailability but also provide a scientific foundation for designing new drug carriers [9]. This, in turn, promotes the development of more efficient and safer drug delivery technologies.

As an emerging biomedical technology, organ-on-a-chip (OOC) integrates the disciplines of micro-nano processing, tissue engineering strategies, and stem cell differentiation technologies to enable the in vitro reconstruction of the complex microenvironments of human tissues and organs. OOC accurately simulates the key structural features and biological functions of target tissues, providing an unprecedented platform for the analysis of physiological mechanisms, simulation of pathological processes, and evaluation of drug efficacy [10–12]. Compared with traditional in vivo studies, OOC enables precise control over biochemical and biophysical cues that are challenging to isolate in living organisms, providing convenience for exploring vascular-related mechanisms [13, 14]. In addition, OOC bypasses the species differences and ethical limitations associated with animal models and maintains human cell specificity. Moreover, constructing an in vitro model using ECs derived from patients to investigate individualized angiogenesis characteristics and drug sensitivity can effectively guide precise treatment [15]. OOC also overcomes the opacity constraints in vivo and can achieve real-time imaging and high-throughput screening of vascular dynamics [16–18]. These features render OOC particularly valuable for systematically deciphering vascular pathophysiology and accelerating therapeutic development.

Currently, for vascularized OOC devices constructed for three-dimensional (3D) cell culture, a physical barrier structure designed based on capillary burst valves is a user-friendly method of achieving hydrogel patterning with applications in the vascularization of tumors [19, 20], bones [21, 22], nerves [23, 24], and cardiac microtissues [25]. As the fluid flows, localized changes in the geometry or material surface properties of the microfluidic channel at the location of the capillary burst valves increase the hydrodynamic resistance, thereby preventing the fluid from advancing. The formation of a high-energy meniscus traps the fluid at this fluid–air interface [26]. The communication pore is designed to connect tissue chambers and medium channels [27, 28]. The Laplace pressure at the gel–air interface, as determined by the contact angle and channel geometry, is optimized to prevent gel bursting. Micropillar arrays can be considered multiple communication pores that allow for an improved efficiency of medium perfusion [29]. Nevertheless, the discontinuity of the ECM–medium interface poses challenges for constructing barrier-like models. To address this issue, microfluidic phaseguide structures with geometric dimensions occupying 25%–50% of the channel height can be implemented. These features exploit the meniscus pinning effect to spatially control hydrogel patterning and also maintain diffusional nutrient exchange with the surrounding culture medium [30, 31]. Despite the accurate design, the physical barrier based on the capillary burst valve has the risk of gel leakage due to high pressures caused by excessive perfusion flow speed [32] and is more susceptible to breakdown at higher channel heights [33]. An injection-molded plastic 3D culture array platform based on rail-guided patterning allows the spontaneous fluid patterning with high repeatability [34–36]. The platform uses the principle of spontaneous capillary flow for fluid loading and the principle of the capillary burst valve to prevent gel leakage at the edges. Nonetheless, scaling up microfluidic architectures for macroscopic tissue models presents challenges, such as elevated structural features (e.g., rails) that reduce Laplace pressure-driven fluid control, often resulting in irregular flow distribution [33].

Currently, most well-established vascularized OOCs are arranged in a single layer, which limits their adaptability and versatility for constructing different tissue models. In contrast, multilayered microfluidic platforms provide significant advantages due to their high flexibility and scalability, allowing the individual design and fabrication of different modules [37]. For instance, a modular microfluidic system with a multilayered configuration was designed for the generation of large-scale vascular networks [38]. However,

to pattern the hydrogel and avoid air bubble trapping, the width of the medium channel openings had to be as small as possible, resulting in semi-closed rhombic medium channels. This design complexity requires extensive prototyping and manufacturing efforts. Moreover, the semi-closed rhombic channels result in inadequate nutrient delivery to tissue chambers, further restricting the practical application of the platform.

In this study, we describe a multilayered microfluidic OOC platform for 3D vascularized microtissue models. Unlike conventional systems, this platform features the bottom channel with multiple branched flow channels functioning as tissue chambers. A porous membrane separates the top channel from the bottom tissue chamber, facilitating robust hydrogel loading and high patterning efficiency. As a proof of concept, we constructed a 3D vascularized model to explore the critical roles of fluidic and biological cues in the vascular formation microenvironment. Furthermore, we successfully replicated the microenvironment of vascularized tumors, simulated key tumor angiogenesis processes, and examined the therapeutic efficacy of antitumor drugs. We also investigated the potential of the multilayered configuration for constructing high-throughput drug screening platforms, emphasizing its design flexibility and scalability. Overall, the proposed multilayered microfluidic chip represents a promising preclinical in vitro platform.

## 2 Materials and methods

### 2.1 Multilayered microfluidic platform fabrication

The molds of the platform were generated using SolidWorks 2023 (Dassault Systèmes, France) and a high-precision 3D printer (Micro-nano 3D printer MP-100-6 L, Prismlab, China). The top and bottom layers were composed of polydimethylsiloxane (PDMS; Sylgard-184, Dow Corning, USA) mixed in a 10:1 (elastomer base:curing agent) mass ratio by soft lithography. The PDMS layers and polyethylene terephthalate (PET) porous membrane were bonded as described previously [39]. The PET membrane was immediately surface-modified with a 2% (volume fraction) aqueous solution of 3-mercaptopropyltrimethoxysilane. After this modification, the membrane was rinsed with distilled water and subsequently dried. The PET membrane was then bonded to the PDMS layers through oxygen plasma treatment. After the completion of the plasma bonding of the three layers, the reservoirs were glued at the ports. The device was autoclaved at 121 °C for 30 min and then sterilized under ultraviolet light for 1 h in a biological safety cabinet.

### 2.2 Cell culture

Red fluorescent protein (RFP)-labeled human umbilical vein endothelial cells (HUVECs) were cultured in endothelial growth medium-2 (EGM-2, Lonza, Switzerland), and 5- to 8-passage cells were used for the experiments. Normal human lung fibroblasts (NHLFs) were expanded in fibroblast medium (FM; ScienCell, USA), and 6- to 9-passage cells were used for the experiments. Human hepatocellular carcinoma (HepG2) cell lines were cultured in minimum essential medium (MEM; Gibco, USA) supplemented with 10% fetal bovine serum (FBS; Adamas Life, Switzerland) and 1% penicillin–streptomycin (Adamas Life). Human nonsmall-cell lung cancer A549 cell lines were cultured in Ham's F-12K medium (Gibco) supplemented with 10% FBS and 1% penicillin–streptomycin. All cells were cultured in a humidified incubator (Thermo Fisher, USA) at 37 °C under 5% $CO_2$. The cells were grown to 80% confluence and then detached from the T25 flasks using 0.25% Trypsin-ethylenediaminetetraacetic acid (Trypsin-EDTA; Adamas Life) for subculture or use.

### 2.3 Spheroid formation

The 3D spheroids were self-assembled in U-shaped 96-well clear ultralow attachment microplates (Corning, USA). Cell suspensions of tumor cells (HepG2 or A549), tumor cells mixed with HUVECs (1:1), and tumor cells mixed with NHLFs (1:1) were prepared at a density of 5000 cells/mL. Then, 200 μL of the cell suspension was added to each well. After preculture for 1–2 d in the microplates, the spheroids were collected for seeding into the microfluidic platform.

### 2.4 Hydrogel-patterning procedures

The fibrin hydrogel was prepared by mixing fibrinogen (5 mg/mL, Sigma-Aldrich, USA) and thrombin (2.5 U/mL, Sigma-Aldrich) dissolved in Dulbecco's phosphate-buffered saline (DPBS; Adamas Life) for all experiments.

For the modeling of vasculogenesis, HUVECs ($5\times10^6$ cells/mL) and NHLFs ($2.5\times10^6$ cells/mL) were harvested and suspended in fibrinogen. After being mixed with thrombin, 25 μL of the cell–gel mixture was injected into the bottom channel until captured by the tissue chambers. Next, air was introduced to remove excess gel from the medium channels. The gel was then crosslinked in an incubator at 37 °C for 10 min. Finally, EGM-2 was added to the medium reservoirs at a static pressure difference of 5 mm $H_2O$. Fresh medium was replaced every 24 h. When replacing the medium, the sides with high and low hydrostatic pressures were switched to reverse the fluidic direction.

For the modeling of angiogenesis, decellularized fibrin gel was loaded and crosslinked. Then, 20 μL of NHLFs ($5\times10^6$ cells/mL) was slowly seeded into the top medium channel. The device was placed in an incubator for 4 h for cell adhesion. Next, 20 μL of HUVECs ($5\times10^6$ cells/mL) was harvested and loaded into the bottom medium channel. The device was placed in an incubator for 1 h at 90 °C to facilitate cell adhesion to the gel surface. Finally, EGM-2 was added to the medium reservoirs and replaced every 24 h.

For the modeling of a vascularized tumor, preprepared tumor hybrid spheroids were homogeneously mixed with decellularized gel and then seeded in the platform. Then, HUVECs ($5\times10^6$ cells/mL) were harvested and loaded into the bottom medium channel. The device was placed in an incubator for 1 h at 90 °C to facilitate adhesion of the cells to the gel surface. Finally, EGM-2 was added to the medium reservoirs and replaced every 24 h.

## 2.5 High-throughput anticancer drug testing procedure

The platform was designed and fabricated as described earlier. HepG2 cells were added to a mixture of fibrinogen and thrombin at a density of $2\times10^6$ cells/mL and loaded into the tissue chambers. Then, a syringe pump (Smith Medical, China) was used to drive both Dulbecco's modified Eagle medium (DMEM) and DMEM containing 10 μmol/L sorafenib into the top concentration gradient generator at a rate of 200 μL/h. The medium was also added to the bottom flow channels.

## 2.6 Finite element analysis

Finite element analysis was performed using the COMSOL Multiphysics 6.0 software (Comsol Inc., Burlington, MA, USA). To improve the computational efficiency, the model was simplified to a chamber cross-section as depicted in Fig. 1d. The decellularized gel was defined as a porous medium with a porosity of 0.99 and a permeability of $1.5\times10^{-13}$ $m^2$, as described previously [27]. For the fluid simulation, the boundary conditions at the inlet and outlet were set to hydrostatic pressures of 6 mm $H_2O$ and 1 mm $H_2O$, respectively, with no viscous stress. The fast laminar flow in the medium channel is described by the Navier–Stokes equations, and the low-velocity flow in the fibrin gel is controlled by the Brinkman equations, which together solve for the continuous velocity and pressure of the same field in the two basins. For the concentration gradient simulation, the boundary conditions at the inlet and outlet were set to 1 and 0 mol/$m^3$, respectively. Fick's law governs the simulations of growth factor transport by migration and diffusion in two-dimensional free and porous media.

## 2.7 Drug treatment

Sorafenib (Adamas Life) was dissolved in dimethyl sulfoxide (DMSO) to prepare a 10 mmol/L stock solution. The stock solution was diluted with EGM-2 to a final concentration of 1 or 10 μmol/L. EGM-2 containing 0.1% DMSO was used in the control experiments.

## 2.8 Imaging and analysis

Cells within the microfluidic platform were imaged and recorded in bright field and fluorescence using an inverted microscope (BZ-X800, KEYENCE, Japan). For the quantitative analysis of vessels, the junction density and average vessel length were analyzed using AngioTool v0.6a (National Cancer Institute), the vessel average area and sprout length were calculated using the ImageJ software (Version 1.51j8, National Institutes of Health, USA), and the vessel diameter is a validated value based on the vessel coverage area and total vessel length. For the quantitative analysis of spheroids, the diameter and area were calculated using the ImageJ software, and the circularity ($C$) was calculated as follows:

$$C=4\pi A/l^2,$$

where $A$ represents the area and $l$ represents the perimeter.

## 2.9 Microbead perfusion

To validate the perfusion of the vascular network, the blue fluorescent 5-μm microbeads were added to the medium in the bottom channel. The hydrostatic pressure of the bottom channel exceeded that of the top channel. The perfusion of microbeads in the vascular network region was recorded using an inverted microscope. For the trajectory tracking of microbeads, the video was extracted as individual frames using Adobe Photoshop 2023 (Adobe, USA) and stacked into a single image using Adobe Premiere Pro 2023 (Adobe).

## 2.10 Statistical analysis

All statistical analyses were conducted using Origin 2022 (OriginLab, USA), and statistical comparisons of the analyzed values were performed using Student's $t$-test. For comparisons involving four or fewer groups, significant pairwise differences are indicated ($^{*}p<0.05$, $^{**}p<0.005$, and $^{***}p<0.0005$). For comparisons involving more than four groups, significant differences between groups are indicated using lowercase letters (e.g., a, b, and c). Groups that do not share the same letter are significantly different ($p<0.05$). The replicate number ($N$) reported in this study represents independent biological replicates, defined as experimental iterations performed using a distinct microfluidic platform

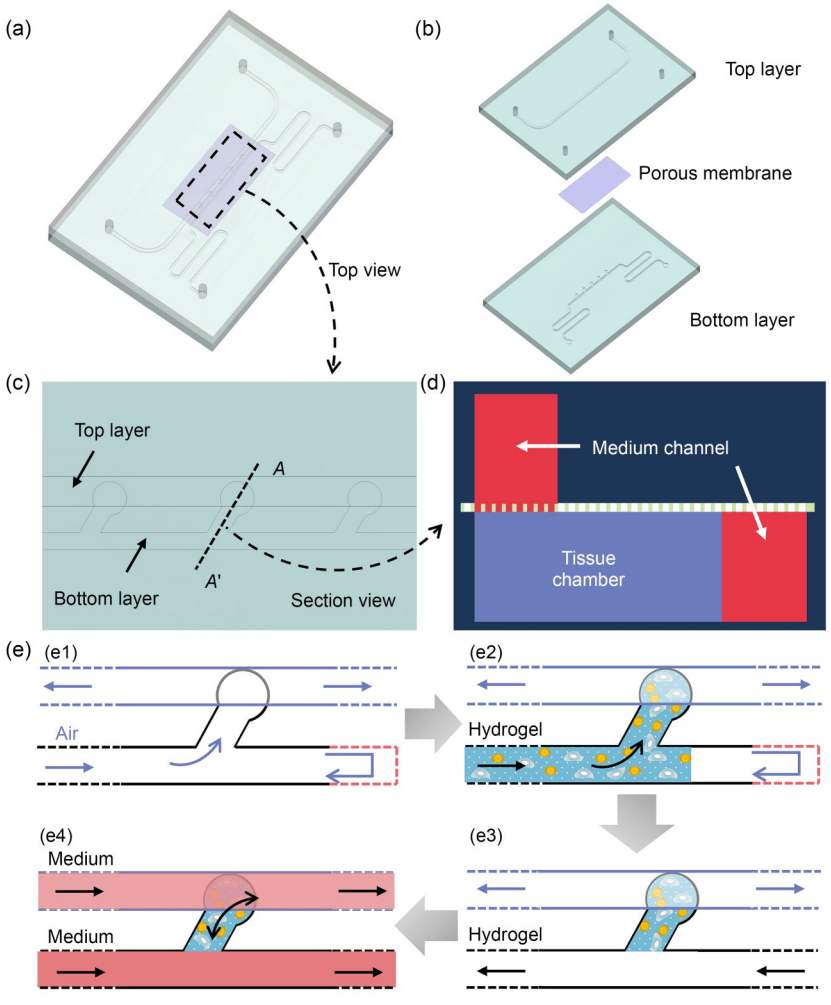


**Fig. 1** Overall schematics of the multilayered microfluidic platform. Assembly (a) and the exploded view (b) of the device. (c) Top view of the culture region with localized detail. (d) The section view of one tissue unit. (e) Schematic of the hydrogel loading procedure: (e1) setting the pressure of the top and bottom medium channel ports; (e2) loading the hydrogel mixed with cells from the inlet of the bottom medium channel; (e3) introducing air to remove the hydrogel from the channel; (e4) introducing the culture medium after crosslinking the hydrogel

to ensure statistical independence and mitigate batch-specific artifacts.

## 3 Results

### 3.1 Design and prototyping of the multilayered microfluidic platform

We designed the multilayered platform, as illustrated in Figs. 1a–1d, consisting of a PDMS top layer, a PET porous membrane layer, and a PDMS bottom layer (structure dimensions of the platform are detailed in Fig. S1 in the supplementary information). The bottom layer features a bottom medium channel with branched channels that serve as tissue chambers. The top channel and tissue chamber are separated by the porous membrane layer, which acts as a hydrogel-patterning barrier to stably prevent capillary-driven hydrogel bursting. Consequently, the contact area between the channels of the multilayered module can be arbitrarily increased according to the design requirements. Each platform contains multiple tissue chambers, providing high flexibility and scalability for generating multiple coupled patterned microtissue models.

We next demonstrated a reliable hydrogel loading procedure that allows the hydrogel to be precisely captured within the tissue chambers (Fig. 1e; Movie S1 in the supplementary information). Initially, the outlet of the bottom medium channel was sealed to ensure high fluid resistance, and the ports of the top medium channel were opened to equalize the atmospheric pressure. Subsequently, the hydrogel was injected into the bottom medium channel. It advanced via capillary action and was captured by the tissue chambers. The introduction of air then removed the hydrogel from the medium channel, thereby retaining a thin layer of hydrogel in the channel that can be used for the EC

lining. A strength of our platform is the robust and adaptable loading procedure, which achieves approximately 100% patterning efficiency in 5 s without the need for precise fluidic control of large equipment.

The parameters of the channel and tissue chambers can be easily modified to accommodate organoid cultures of different sizes. The entrance width of the tissue chamber significantly influenced the hydrogel-filled area and the filling area ratio (Fig. S2 in the supplementary information). The results indicated that a larger entrance width yields a lower filling area ratio. Furthermore, the flow resistance of the hydrogel into the tissue chamber increased considerably with the decrease in the entrance width (smaller than the width of the bottom channel). Based on the experimental results, the bottom medium channel was designed with a width and height of 300 μm, whereas the entrance width was set at 400 μm for the construction of the vascularization model.

## 3.2 Determination of optimal interstitial flow conditions for stimulating vasculogenesis

As depicted in Fig. 2a, the interstitial flow (IF) across the tissue chambers was simply established by setting a hydrostatic pressure difference between the top and bottom medium channels. This hydrostatic pressure can be regulated to generate a physiological flow range conducive to vasculogenesis. To identify hydrostatic pressure conditions that favor vasculogenesis, the time-dependent evolution of the hydrostatic pressure difference was experimentally characterized by setting the initial hydrostatic pressure differences of 5, 10, and 20 mm $H_2O$, as illustrated in Fig. 2b. The results revealed a "fast followed by slow" trend, with an initially rapid decline in pressure difference followed by a slower phase over time. To maintain adequate interstitial fluid stimulation within the tissue lumen, the pressure difference was adjusted every 24 h. According to the fluid continuity equation, the temporal rate of change in the hydrostatic pressure difference is proportional to the interstitial fluid flow rate within the tissue chamber (see the supplementary information for detailed derivations and calculations). Based on this relationship, the average IF velocities across the tissue chambers corresponding to each initial pressure condition were calculated from the experimentally measured pressure differences, as depicted in Fig. 2c. Under the 5 mm $H_2O$ hydrostatic pressure difference condition, the IF velocity decreased from 9.59 to 3.48 μm/s, remaining within the optimal range reported to induce vasculogenesis [40], whereas the IF velocity driven by 10 mm and 20 mm $H_2O$ hydrostatic pressure differences exceeded this range.

The above-reported IF velocity represents the average flow rate within the defined cross-section of the tissue chamber. To further explore the spatial distribution of fluid flow within the tissue chamber, we conducted a detailed analysis using finite element modeling implemented in the COMSOL Multiphysics 6.0 software. To improve the computational efficiency, the material in the tissue chamber

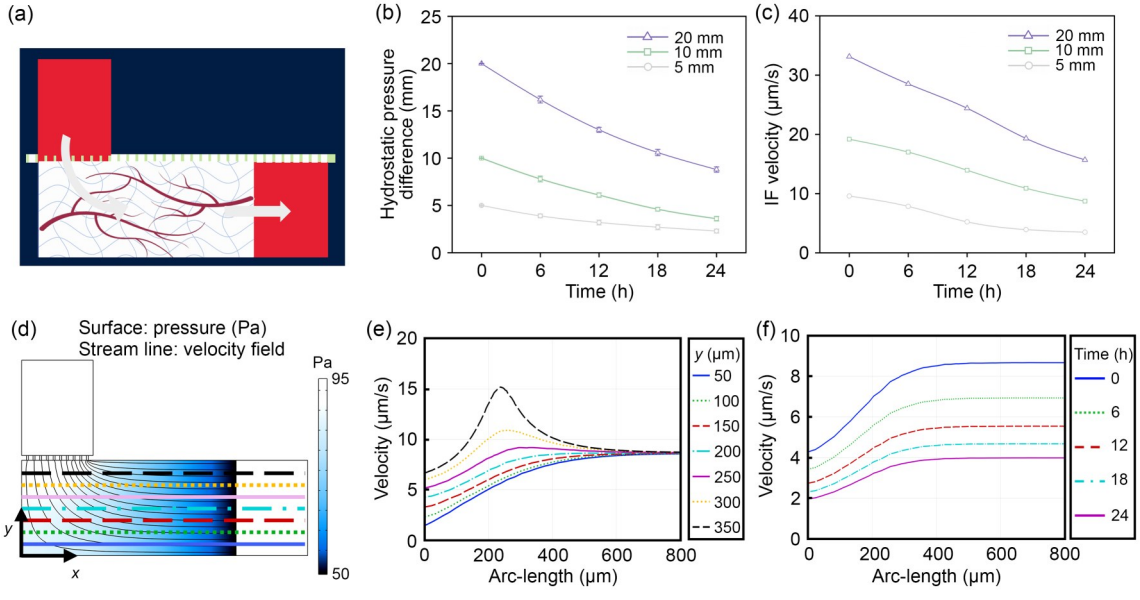


**Fig. 2** Spatial and time-dependent simulation results of IF across the tissue chamber required for inducing vasculogenesis. (a) Schematic of vasculogenesis under the IF between the top and bottom layers. (b) Sample curve based on the experimental results of the decrease of the hydrostatic pressure difference under the initial pressure differences of 5, 10, and 20 mm $H_2O$ over 24 h ($N$=3). All data are expressed as mean±standard deviation. (c) Average IF speed within the tissue chamber calculated from the experimental results over 24 h. (d) Simulated hydrostatic pressure distribution (slice) and IF velocity field (stream line). (e) Simulation results of the IF velocity of $y$-direction lines (the format of the lines corresponds to the cut lines in (d) across the tissue chamber). (f) Time-dependent simulation results across the tissue chamber from time $t$=0 h to $t$=24 h

was set up as a decellularized fibrin gel, and the fluid flow was driven by a 5 mm $H_2O$ hydrostatic pressure difference between the top and bottom channels. The identical pressure difference between the entry and exit of each tissue chamber resulted in the same flow field distribution in each chamber. The slices represent the pressure distribution, and the streamlines indicate the IF velocity field (Fig. 2d). In addition, the flow velocity variations along the profile lines at different heights were examined to adequately quantify the flow in different regions across the tissue chamber. Due to the asymmetric distribution of flow resistance, the flow velocity increased along the *y*-direction, and was higher in the central region than in the peripheral region (Fig. 2e). The overall flow velocity range was within 1–15 μm/s. Figure 2f illustrates the simulated results of IF velocity across the tissue chamber, which decreased from 7.67 μm/s at 0 h to 3.53 μm/s at 24 h, a value that is almost similar to the range of variation of the measured average IF velocity [40]. Therefore, we conclude that the 5 mm $H_2O$ hydrostatic difference between the top and bottom channels was reset every 24 h to maintain adequate IF stimulation across the tissue chamber. Because ECs sense shear stress and sprout in the opposite direction of flow [41], circulating fluid stimuli were established between the top and bottom channels.

## 3.3 Modeling of 3D vasculogenesis under IF conditions

Fibrinogen and thrombin mixed with RFP-labeled HUVECs and NHLFs were loaded into the multilayered microfluidic platform according to the established loading procedure. After 10 min of hydrogel crosslinking, IF crossing through the tissue chambers was initiated by perfusion with EGM-2. As early as Day 1, HUVECs began to interconnect, forming vascular fragments. By Day 5, the vascular fragments had continued to anastomose and lumenize (Fig. 3a). As depicted in Fig. 3b, the confocal image demonstrated localized vascular network distribution within the tissue lumen, suggesting a vascular luminal structure and interconnected network. To confirm the continuous lumen structure and perfusable functionality of the vascular network, 5-μm microbeads were perfused into the platform (Movie S2 in the supplementary information), demonstrating their movement through the lumens along the vascular networks. This result confirms the transition from 3D-cultured HUVECs to lumenized vascular networks. There was also a tendency for HUVECs to migrate outward to the bottom medium channel against the flow direction. Quantitative analysis of the vessel coverage area, average vessel length, junction density, and vessel diameter is presented in Figs. 3c–3f. The vessel coverage area and junction density decreased with the increase of culture time, indicating improved interconnection of HUVECs and anastomosis between vessel fragments. Conversely, the average vessel length and diameter increased with culture time, suggesting that the vessel fragments gradually developed into a mature and perfused microvascular network under the stimulation of IF and fibroblast support.

## 3.4 IF affects the structure of vasculogenesis on the platform

To further investigate the effect of IF on vasculogenesis, the tissue chamber was divided into two regions of interest (ROIs) for study, viz., a head region with a larger circular shape and a narrower neck region (Fig. 4a). We detected an inhomogeneous IF generated according to Bernoulli's principle governing fluid dynamics equation. We used the COMSOL Multiphysics software to calculate the average flow velocities in the head and neck regions and observed 52% higher flow velocities in the neck region than in the head region (neck: 8.5 μm/s, head: 5.6 μm/s; under 5 mm $H_2O$ hydrostatic pressure). We subsequently quantified the differences in the vessel coverage area, junction density, and vessel diameter in the two regions (Figs. 4b–4d). Overall, the vascular network formation at higher IF rates showed larger vessel diameters, smaller coverage areas, and lower junction densities than the vascular network formation at lower IF rates, suggesting that a more robust and better perfused vascular network was formed at high IF rates. Furthermore, the global vascular network structure can be regulated by controlling the difference in the hydrostatic pressure.

## 3.5 Modeling of angiogenesis under the paracrine effect of stromal cells on ECs

When modeling vasculogenesis, mixed cultures of HUVECs and NHLFs obscured the findings related to direct or indirect contact interactions [42]. To address this issue, porous membranes serve as physical barriers that create a distinct separation between the top and bottom layers. Using this multilayered platform, stromal cells can be cultured in the top channel, and the thin hydrogel layer after decellularized gelatin in the bottom channel can be used for EC lining (Fig. 5a). For angiogenesis modeling, NHLFs act as stromal cells, secreting growth factors that induce the sprouting of HUVECs toward regions of high growth factor concentrations. Finite element analysis revealed the formation of a smooth growth factor concentration gradient across the tissue chamber, with a mean concentration of 49% and a concentration gradient of 0.056%/μm (Figs. 5b and 5c). After ECs lined the channel, a dense monolayer gradually formed in the bottom channel. The paracrine effect of NHLFs induced the HUVECs to sprout into the chambers, generating the vasculature with a clear lumen by Day 9 (Fig. 5d). The simulation results also revealed a vertical gradient in the

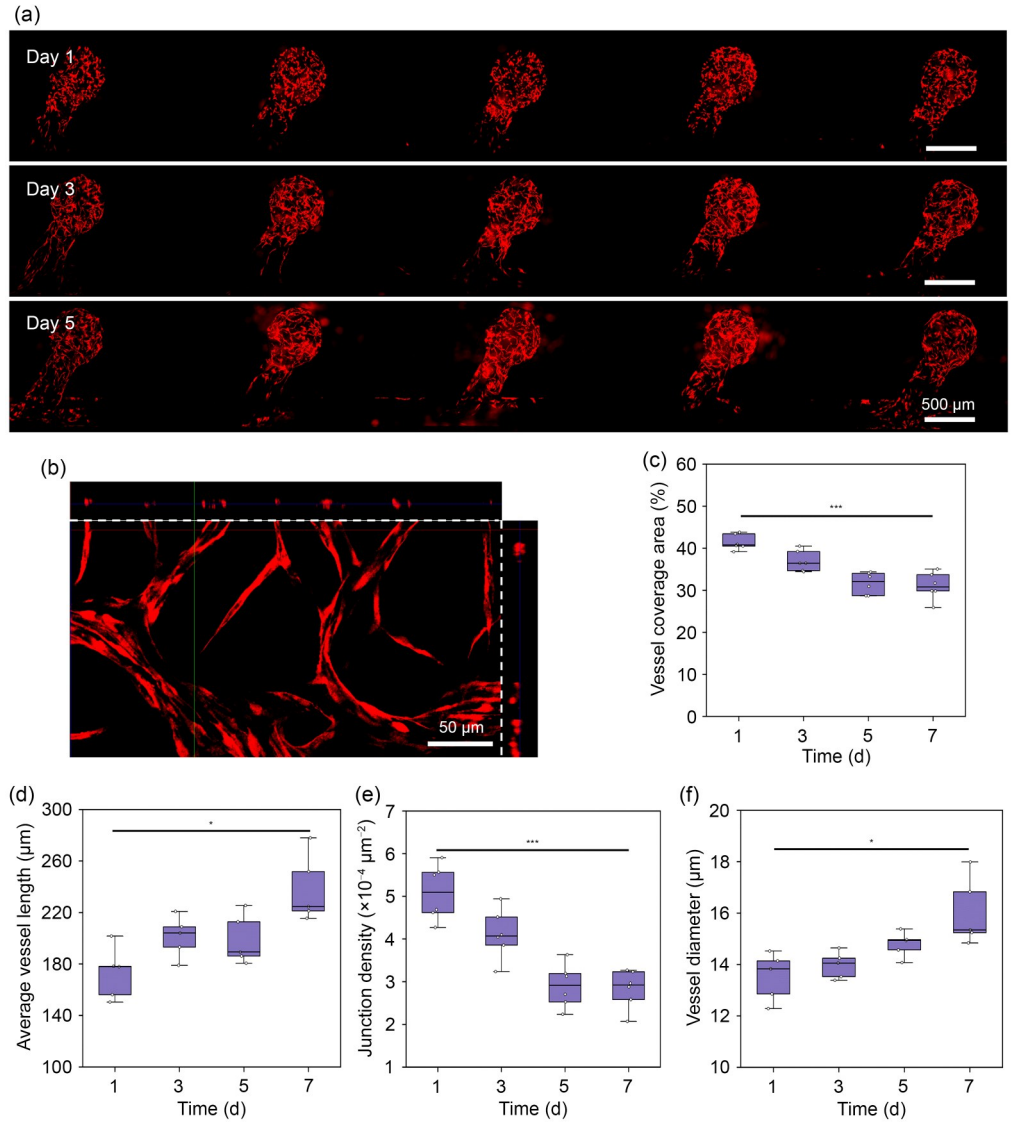


**Fig. 3** Generation of 3D vascular networks through vasculogenesis with IF stimulation. (a) Process of vasculogenesis on the platform from Day 1 to Day 5. (b) Confocal fluorescence image of the local microvascular network at the tissue chamber. Quantitative analysis of the vessel coverage area (c), average vessel length (d), junction density (e), and vessel diameter (f) with culture time ($N$>5). Data are expressed as mean±standard deviation. $^{*}p$<0.05, $^{***}p$<0.0005

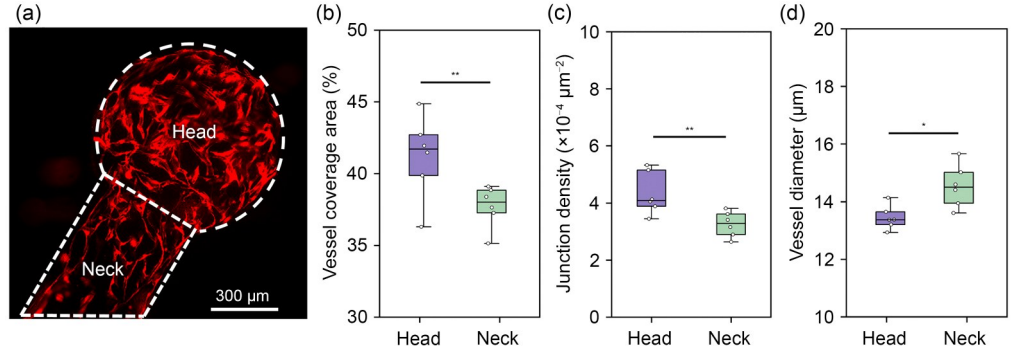


**Fig. 4** IF improves the structure of vascular networks through vasculogenesis. (a) Segmentation of the tissue chamber into two ROIs according to the geometry for analysis, viz., the head and neck regions. Statistical analysis of the vessel coverage area (b), junction density (c), and vessel diameter (d) in the head or neck region on the platform under 5 mm $H_2O$ hydrostatic pressure ($N$=6). Data are expressed as mean±standard deviation. $^{*}p$<0.05, $^{**}p$<0.005

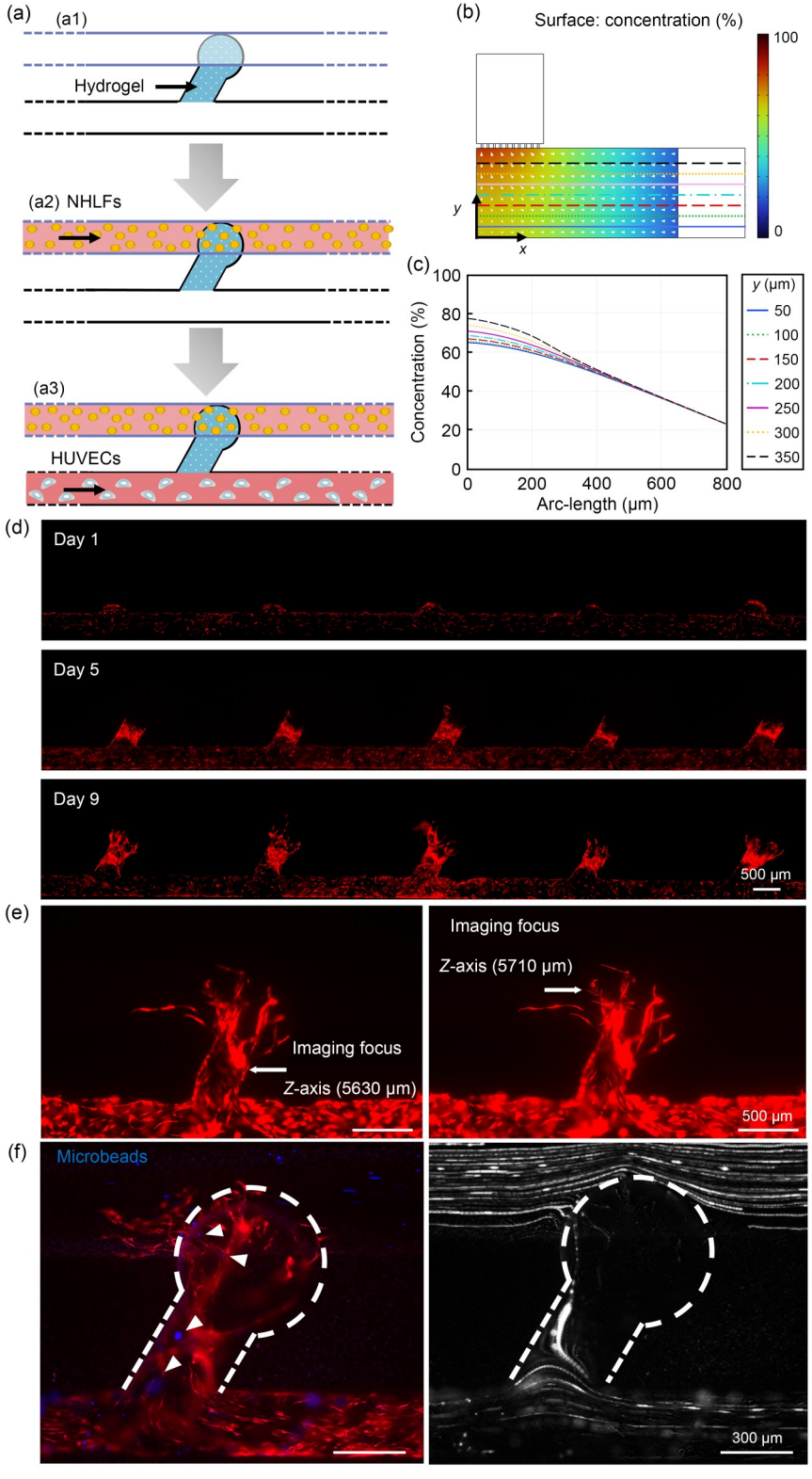


**Fig. 5** Overview of the angiogenesis model under the paracrine effect of stromal cells. (a) Schematic of the hydrogel loading procedure for modeling angiogenesis: (a1) loading the decellularized hydrogel; (a2) seeding the NHLFs into the top medium channels; (a3) seeding the HUVECs into the bottom channels. (b) Simulated growth factor concentration distribution (slice) and direction of concentration gradient (arrow). (c) Simulation results of the growth factor concentration of *y*-direction lines (the line format corresponds to (b) across the tissue chamber). (d) Process of angiogenesis on the platform from Day 1 to Day 9. (e) Images of different layer heights indicating the growth of vessels in the vertical direction. (f) Image stack for frame-by-frame (355 frames) tracking of flowing microbeads (blue: microbeads; red: HUVECs), highlighting the tracks of the microbeads passing through the perfusable vessels

distribution of the growth factor concentration, which was corroborated by the observed vessel structure. As depicted in Fig. 5e, the root of the vessel was 80 μm below the tip of the vessel by adjusting the focal view plane. Moreover, the vessel emerged upward until it passed through the porous membrane and entered the NHLF regions after prolonged culture. To illustrate the perfusability of the vascular network, fluorescent microbeads were perfused in the bottom channel, and their trajectories were synthetically tracked to characterize the flow within the model of angiogenesis. Some microbeads entered the sprouting vessels from the bottom medium channel and moved into the top medium channel (Fig. 5f; Movie S3 in the supplementary information). Because the lumen of the vessels was much narrower than that of the medium channel, which caused high flow resistance, only a few microbeads flowed through the vessels at a low speed. Consequently, the fluorescence intensity of the microbead trajectories was higher in the channel than in the vessel region.

## 3.6 NHLFs control the sprouting vessel morphology through paracrine effects

Under normal physiological conditions, fibroblasts play a vital role in regulating the secretion of essential growth factors and chemokines to improve angiogenesis [43]. This paracrine promotion of ECs by fibroblasts exerted a dose-dependent effect. As depicted in Fig. 6a, NHLFs were seeded at high ($10^7$ cells/mL) or low ($10^6$ cells/mL) density in the top medium channel to induce the sprouting of HUVECs. On Day 1, statistical analysis revealed significant differences in the area and length of the vasculature induced by fibroblasts of varying densities. By Day 9, both the coverage area and vessel length induced by high-density NHLFs exceeded those induced by low-density NHLFs (Figs. 6b and 6c). These findings demonstrate the vital role of fibroblasts as stromal cells in maintaining and promoting the growth of the vascular network.

## 3.7 Construction of a 3D vascularized tumor model on the platform

The growth, invasion, and metastasis of tumors are dependent on the process of tumor vessel formation [44, 45]. In the primary TME, tissues secrete hypoxia-inducible factors and growth factors that stimulate the recruitment of ECs and the formation of new blood vessels from the existing vascular network, thereby establishing its own microcirculation system [46, 47]. 3D tumor spheroid models can be assembled using U-shaped 96-well clear ultralow attachment microplates to simulate compact tumor tissue in vivo. The size of these spheroids was modified by controlling the

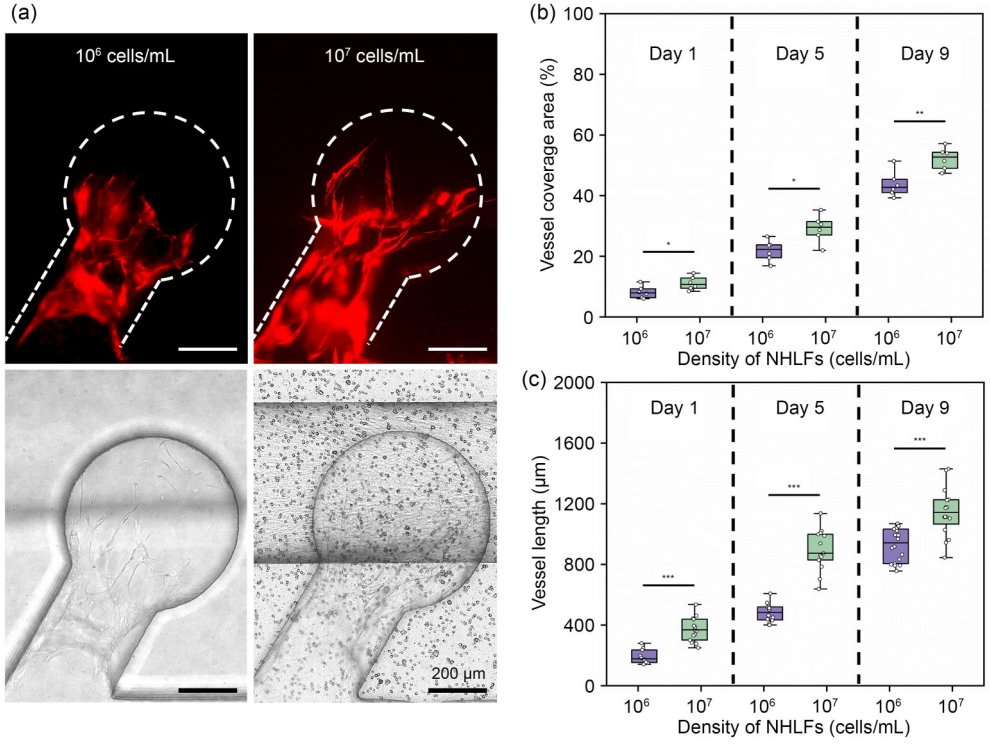


**Fig. 6** Quantification of paracrine effects of NHLFs according to vascular morphology. (a) Fluorescence and bright-field images of vascular sprouts induced by NHLFs with different initial seeding densities (high: $10^7$ cells/mL; low: $10^6$ cells/mL) at Day 9. Statistical analysis of the vessel coverage area (b) and vessel length (c) of the vascular sprouts by two initial seeding densities of NHLFs with the culture time ($N$>6). Data are expressed as mean±standard deviation. $^{*}p$<0.05, $^{**}p$<0.005, $^{***}p$<0.0005

density of HepG2 cells (Figs. S3a and S3b in the supplementary information), and spheroids with a diameter of <600 μm maintained high viability (Fig. S3c in the supplementary information). The co-culture of tumor cells and stromal cells into spheroids facilitates the generation of more physiologically representative tumor microtissues [48]. Tumor–stromal hybrid spheroids were assembled by mixing HepG2 cells with NHLFs or HUVECs using a total of 1000 cells in a 1:1 ratio. As illustrated in Fig. S4 (supplementary information), hybrid HepG2 cells mixed with NHLFs exhibited a reduction in size and an improvement in circularity compared with HepG2 spheroids alone. In contrast, HepG2 cells mixed with HUVECs could not aggregate into clusters to maintain a spherical shape. This observation suggested that the addition of NHLFs improved the self-assembly efficiency of HepG2 cells, resulting in denser spheroids. Furthermore, the incorporation of NHLFs improved the capacity to induce angiogenesis. To design the vascularized liver tumor model on the platform, fibrin gel mixed with hybrid spheroids (HepG2 cells and NHLFs) was injected into the platform. The bottom medium channel was then lined with HUVECs to mimic the macrovessels (Fig. 7a). With the induction of hybrid tumor spheroids, HUVECs sprouted toward the tumor spheroids, forming substantial contact (Fig. 7b). To validate the robustness of our multilayered microfluidic platform for constructing vascularized tumor models, we induced tumor angiogenesis using hybrid spheroids composed of A549 cells and NHLFs (a total of 1000 cells, in a 1:1 ratio, Fig. 7c). Our results demonstrated consistent vascular network formation that exhibited a preferential orientation toward the tumor region. This model thus provides a more accurate representation of the TME and its vascularization processes.

The biomechanical properties of the ECM, particularly stiffness, serve as critical regulators of tumor progression and angiogenic dynamics [49]. To explore the contribution of ECM stiffness to tumor proliferation and vascular formation, stiffness conditions were constructed by modulating the fibrin gel concentrations, categorized into low (3 mg/mL), moderate (6 mg/mL), and high (12 mg/mL) groups. As illustrated in Fig. 7d, tumor vascular sprouting was induced under low and moderate stiffness conditions after 5 d of

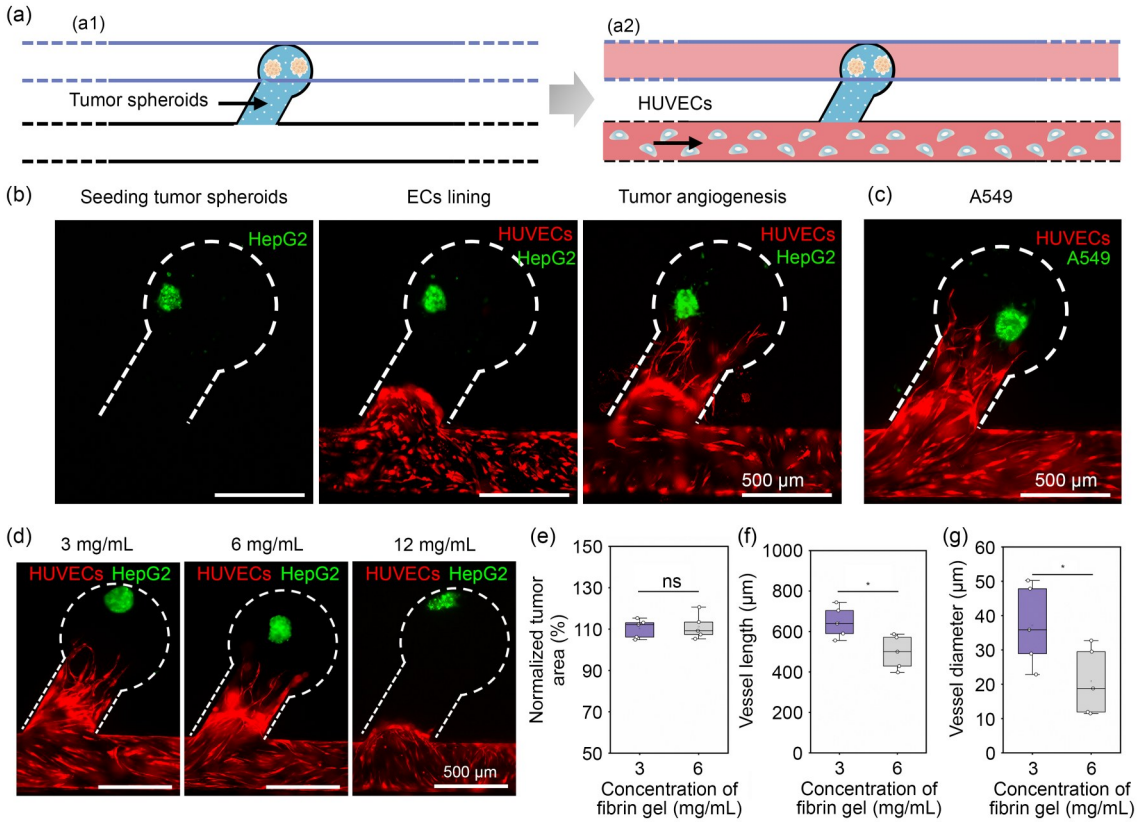


**Fig. 7** Recapitulation of a 3D vascularized tumor through angiogenesis in vitro. (a) Schematic of the hydrogel loading process for modeling the vascularized tumor: (a1) loading the hydrogel mixed with tumor hybrid spheroids; (a2) seeding the HUVECs into the bottom medium channel. (b) Representative fluorescence images of the tumor vascular formation process (HepG2: green; HUVECs: red). (c) Representative fluorescence image of vascularized A549 tumor hybrid spheroids (A549: green; HUVECs: red). (d) Representative fluorescence images of vascularized tumor models at 3, 6, and 12 mg/mL fibrin gel concentrations (HepG2: green; HUVECs: red). Quantitative analysis of tumor size (e), vessel length (f), and vessel diameter (g) in different fibrin gel concentrations ($N$=5). Data are expressed as mean±standard deviation. ns: not significant; $^{*}p<0.05$

culture, whereas no vascular sprouts were observed under the high stiffness condition. Quantitative morphological analysis revealed no statistically significant difference in tumor size among the groups (Fig. 7e). Moreover, under a low fibrin concentration of 3 mg/mL, sprouted vessels averaged 646.50 μm in length and 37.14 μm in diameter. In contrast, a moderate fibrin gel concentration of 6 mg/mL resulted in the formation of shorter and narrower sprouted vessels (Figs. 7f and 7g).

### 3.8 Analysis of sorafenib efficacy in the replication of early/terminal liver cancer therapy

Sorafenib, an anticancer drug approved by the Federal Drug Administration (FDA), is the gold standard for the treatment of advanced liver cancer. It targets Raf serine/threonine kinases and receptor tyrosine kinases, including vascular endothelial growth factor receptors 1, 2, and 3, as well as platelet-derived growth factor-β, Flt-3, and c-kit [50]. To determine the efficacy of sorafenib, we initially treated HepG2 hybrid spheroids with varying doses of sorafenib in the well plates. The proliferative size of tumor spheroids was significantly inhibited after treatment with 1 and 10 μmol/L doses of sorafenib compared with that in the control group (Fig. S5 in the supplementary information). In addition, live/dead staining analysis revealed a dose-dependent pattern of cellular mortality in sorafenib-treated tumor hybrid spheroids (Fig. S6 in the supplementary information). Therefore, the efficacy of anticancer drugs can be evaluated by determining the size and mortality of tumor spheroids. Subsequently, we reconstructed the 3D vascularized liver tumor model on the platform to simulate early and terminal tumors based on prevascularization and post-vascularization stages. For early treatment (Figs. 8a–8c), sorafenib was administered into the ECs-lined channels mimicking large blood vessels on Day 1, and the drug was renewed every 24 h for 7 d. Results showed that sorafenib significantly reduced the growth of tumor hybrid spheroids in a dose-dependent manner, while both 1 and 10 μmol/L doses inhibited the initiation of angiogenesis. For terminal treatment (Figs. 8d–8f), sorafenib was introduced to the model after 7 d of tumor-induced angiogenesis and maintained for 3 d. Compared with that in the control group, the relative tumor area was also reduced in the drug trial group. There was no significant change in the vessel coverage area after 1 μmol/L sorafenib treatment, whereas 10 μmol/L sorafenib treatment induced apoptosis in the vascular network. We next examined the effects of sorafenib on the viability of HUVECs (Fig. S7 in the supplementary information) and found that 1 μmol/L sorafenib treatment exhibited no significant cytotoxicity in HUVECs; however, it significantly inhibited the initiation of tumor angiogenesis, thereby simulating early treatment. These findings suggest that sorafenib exerts a more potent antiangiogenic effect than direct cytotoxic activity at lower concentrations. In contrast, treatment with 10 μmol/L sorafenib induced substantial cytotoxicity, consistent with the apoptotic effects observed in vascular networks in terminal treatment at high drug doses.

We also observed that tumor spheroids cultured on the platform were more sensitive to sorafenib treatment than spheroids cultured on microplates (Fig. 9). Moreover, the relative size of tumor spheroids after 1 or 10 μmol/L sorafenib terminal treatment was smaller than those observed during early-stage treatment (1 μmol/L: (90.6±3.49)% vs. (95.08±3.15)%; 10 μmol/L: (82.06±3.00)% vs. (89.80±2.36)%), respectively, with statistically significant differences. The results demonstrate the importance of the microvascular network in antitumor drug delivery. Overall, these findings support the antitumor profile of sorafenib and demonstrate the functionality of our multilayered microfluidic platform for vascularized tumor construction and anticancer drug efficacy assessment.

### 3.9 Multilayered microfluidic platform for high-throughput anticancer drug testing

To validate the flexibility and scalability of our multilayer configuration design, we decoupled the top and bottom layers of the platform. This decoupling allowed for the expansion of the number of tissue chambers in the bottom layer. The top layer was designed as the classic Christmas-tree structure to generate the drug concentration gradient, with fluid from the top channels diffusing into the bottom tissue chambers (Fig. 10a). To calibrate the concentration gradient generated by the Christmas-tree structure, a fluorescence intensity gradient was established using fluorescein isothiocyanate (FITC)-dextran. PBS and PBS containing 50 μg/mL FITC-dextran were introduced into the two inlets at a flow rate of 2 μL/h using a syringe pump (Fig. 10b), and the resulting fluorescence intensity gradients in the five channels were 0.03%, 18%, 44.3%, 78.4%, and 99.5%, respectively (Fig. 10c). Subsequently, a series of sorafenib concentration gradients was generated and applied to the 3D HepG2 cultures in the bottom layer. Figures 10d and 10e show the effect of sorafenib concentration gradients on the viability of HepG2 cells. Sorafenib effectively inhibited the proliferation of HepG2 cells in a dose-dependent manner according to the relative tumor area and drug concentration. Furthermore, the morphological analysis revealed cellular shrinkage in the tumor cells after drug treatment, consistent with the typical characteristics of programmed apoptosis. These findings suggest that sorafenib induces HepG2 cell death by activating the apoptotic pathway. To summarize, this device has significant utility for high-throughput anti-drug screening.

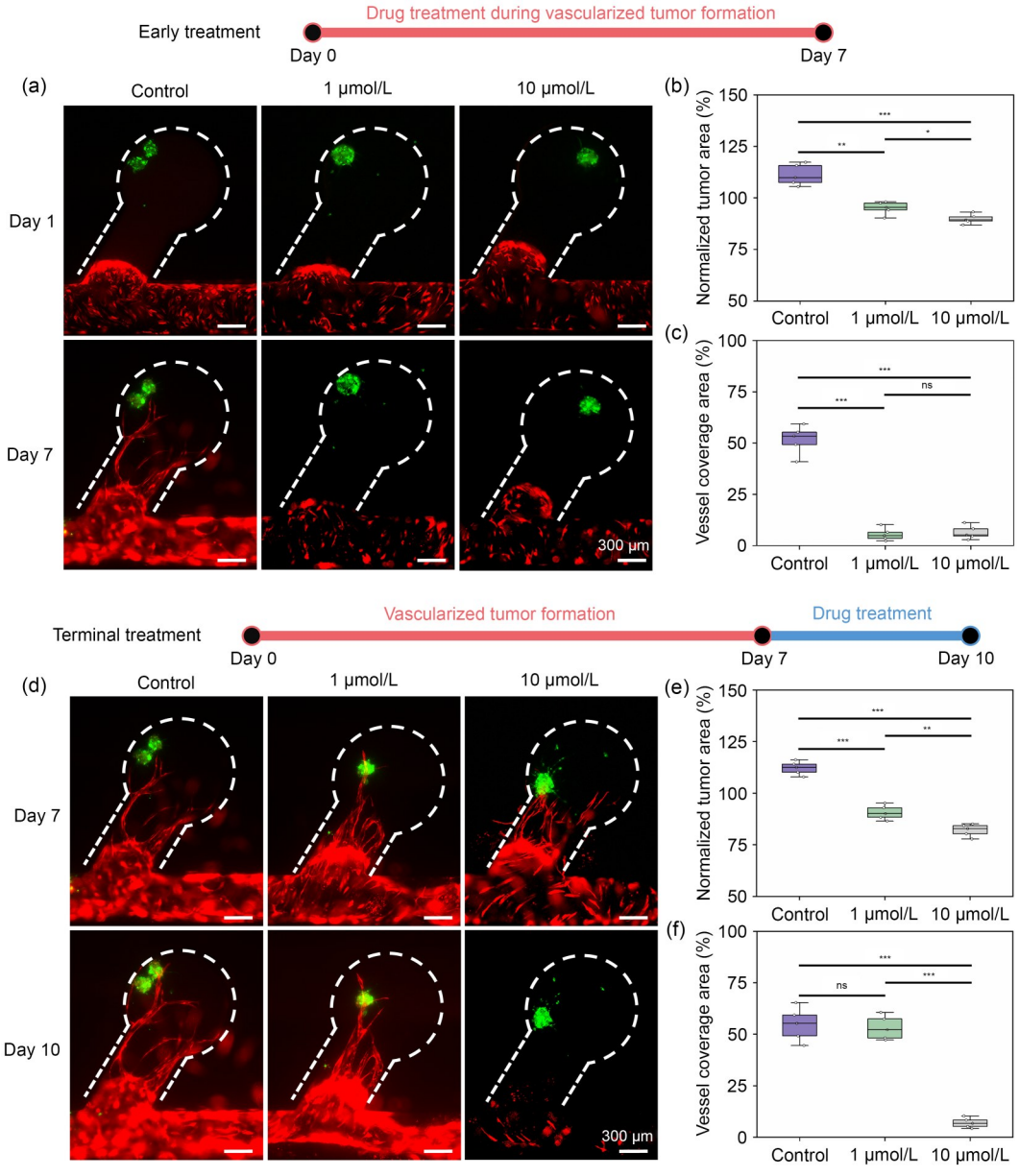


**Fig. 8** Evaluation of anti-liver cancer drugs in the vascularized tumor model in vitro. For early treatment, sorafenib was introduced into the model from Day 0 to Day 7. (a) Representative fluorescence images demonstrating the response of tumor spheroids and vascular tissue to different concentrations (1 μmol/L and 10 μmol/L) of sorafenib treatment on Day 1 and Day 7 (HepG2: green; HUVECs: red). Statistical analysis of normalized tumor area (b) and vessel coverage area (c) on Day 7 ($N$=5). For terminal treatment, sorafenib was administered into the model from Day 7 to Day 10. (d) Representative fluorescence images demonstrating the response of tumor spheroids and vascular tissue to different doses of sorafenib treatment on Day 7 and Day 10 (HepG2: green; HUVECs: red). Statistical analysis of normalized tumor area (e) and vessel coverage area (f) on Day 10 ($N$=5). Data are expressed as mean±standard deviation. ns: not significant; $^{*}p<0.05$, $^{**}p<0.005$, $^{***}p<0.0005$

## 4 Discussion

In this paper, we present a multilayered microfluidic platform that provides a simple and robust procedure for establishing vascularized OOC models. A key innovation of this platform is the use of a porous membrane as a hydrogel anchoring interface, which effectively addresses the issue of hydrogel leakage associated with the capillary burst valve phenomenon [27, 28]. Compared with the previously reported multilayer vascularization system [38], this design not only ensures that the hydrogel is stably and precisely anchored at the porous membrane interface, but also enhances contact between the hydrogel and culture media in the top and bottom channels, thereby enabling efficient exchange of nutrients, oxygen, growth factors, and waste products. Moreover, this robust design overcomes the challenge of insufficient tissue height observed in existing chip designs. Furthermore, the physical barrier effect of the porous

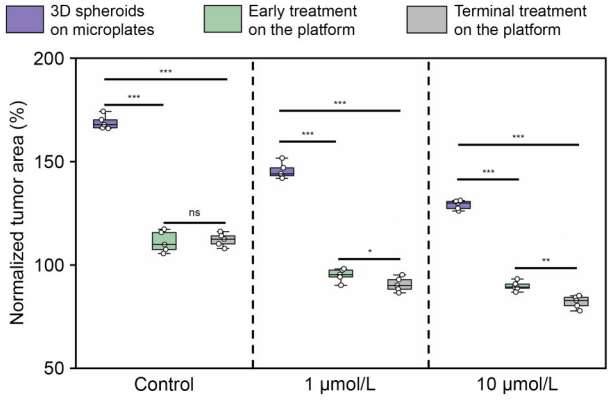


**Fig. 9** Quantification of normalized tumor area under treatment with 0, 1, and 10 μmol/L sorafenib with 3D spheroids on microplates, early treatment, and terminal treatment on the platform ($N$=5). Data are expressed as mean±standard deviation. ns: not significant; $^{*}p<0.05$, $^{**}p<0.005$, $^{***}p<0.0005$

membrane separation can be used to explore the paracrine effects of different cultured cells in the top and bottom layers.

This multilayered microfluidic platform facilitates the bottom-up generation of homogeneous and dense vascular networks, closely mimicking the in vivo development of capillary networks through processes such as vasculogenesis and angiogenesis. Our study demonstrated that vascular morphogenesis was influenced by mechanical and biochemical factors. Specifically, increased IF results in an increased vessel diameter, reduced vessel coverage, and fewer junctions, thereby contributing to the formation of a more mature vascular network. IF upregulates matrix metalloproteinase-2 (MMP-2) expression and promotes angiogenesis in ECs [51]. In addition, shear stress augments nitric oxide release from ECs, thereby supporting vasodilation [52]. High growth factor levels promote angiogenesis, which is consistent with previous findings on the promitotic and antiapoptotic effects of growth factors on ECs [53].

To validate the vascularized organ model, we developed a 3D vascularized tumor spheroid model that accurately recapitulates primary tumor angiogenesis and allows for the characterization of the tumor tissue microenvironment and its microphysiological functions. We observed that ECM stiffness significantly modulated the morphological characteristics of tumor-induced vessels. A comparative analysis revealed that 3D cultures in 6 mg/mL fibrin hydrogels generated vascular outgrowths with reduced total length and diminished lumen diameter compared with those of cultures in 3 mg/mL fibrin gel. This result is consistent with a previous report [54], suggesting that the force generated by ECs is insufficient to effectively penetrate a more mechanically resistant and less porous ECM [55]. Moreover, the increased stiffness of the ECM renders it more resistant to proteolytic degradation and impedes the migration of ECs. Previous studies reported that increased ECM stiffness induced abnormal tumor vascular remodeling, characterized by structural deformities and compromised vessel wall

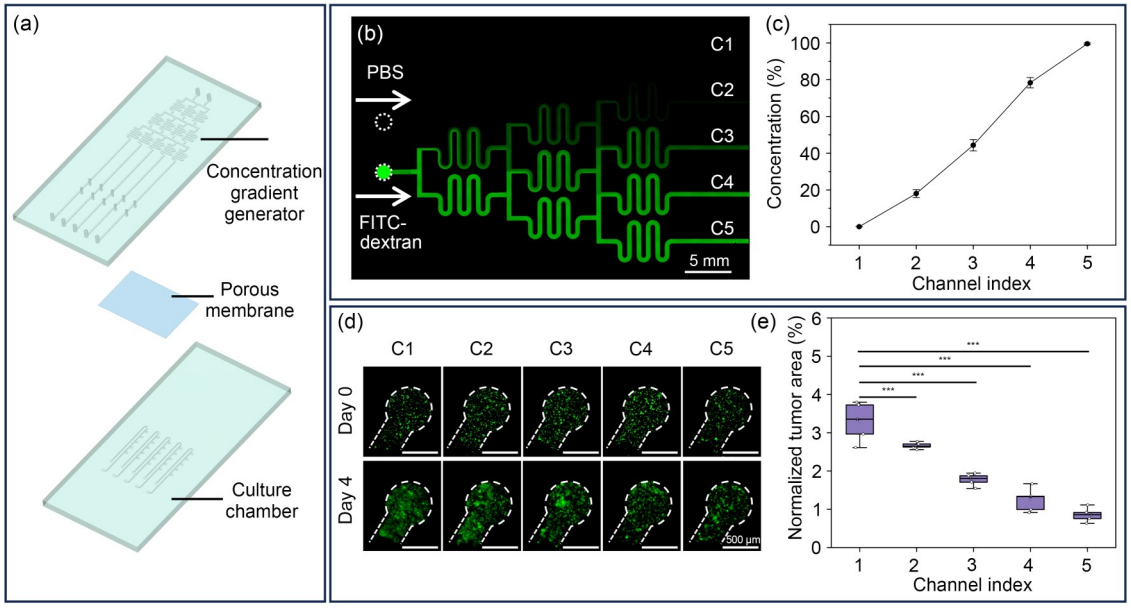


**Fig. 10** Multilayered microfluidic platform for high-throughput anticancer drug testing. (a) Schematic of the high-throughput platform with the top Christmas-tree structure for concentration gradient generation and the bottom layer for multitissue culture. (b) Concentration gradient of FITC-dextran in the top layer. (c) Quantification of the concentration gradient of FITC-dextran in the top layer ($N$=3). (d) Viability of HepG2 cells exposed to sorafenib at varying concentrations (0–10 μmol/L) on the platform from Day 0 to Day 4 in 3D culture. (e) Quantification of normalized tumor area for HepG2 cells exposed to sorafenib at varying concentrations ($N$=5). Data are expressed as mean±standard deviation. $^{***}p<0.0005$

stability [56]. Our experimental results revealed no statistically significant association between matrix stiffness and primary tumor size. Nevertheless, ECM stiffness is known to play a vital role in tumor proliferation, invasion, and metastasis [49, 57]. Mechanistically, increasing the ECM stiffness induces proliferative responses in HepG2 cells through the coordinated activation of extracellular regulated kinase (ERK), protein kinase B (PKB/Akt), and activator of transcription 3 (STAT3) signaling cascades [58]. Furthermore, the biomechanical analysis indicated that ECM rigidity directly modulates transforming growth factor-β (TGF-β) signaling dynamics, thereby promoting epithelial–mesenchymal transition [59].

Our study demonstrated the dual therapeutic mechanism of antitumor and antivasculature activity of sorafenib across tumor vascularization stages, concurrently exhibiting endothelial cytotoxicity and antiangiogenic properties across different concentration thresholds. A comparative pharmacodynamic evaluation revealed increased drug sensitivity of tumor models in microfluidic platforms compared with that of conventional well plate models. This phenomenon occurs because tumor spheroids cultured on microplates exhibited accelerated proliferation rates that exceeded the threshold for drug inhibition, a result attributed to low mechanical constraints in the ECM-deficient environment and sufficient oxygen and nutrients [60]. Conversely, platform-based models recapitulated the in vivo-like growth equilibrium through ECM-mediated physical constraints that restricted cellular migration and proliferative expansion. Therapeutic simulation experiments revealed critical temporal dependencies, where early treatment models demonstrated inefficient drug permeation depending solely on concentration gradient diffusion [61], whereas vascularized models simulating terminal treatment facilitated improved drug delivery through established vascular networks. The drug penetration efficiency in vascularized systems is amplified by pathological vascular abnormalities and drug-induced endothelial barrier disruption [20]. These findings confirm that vascularized TMEs with functional microcirculatory networks provide superior biomimetic platforms for simulating in vivo pharmacokinetic profiles.

Compared with traditional single-layer chip designs, the multilayered design provides significant advantages in terms of design flexibility and scalability by allowing the decoupling of the top and bottom layers. For the bottom layer, the structure of the tissue chambers can be easily modified to accommodate microtissue or organoid cultures of various sizes. Moreover, the number of tissue chambers can be expanded to produce a large-scale OOC platform. Multiple rows of tissue chambers can be interconnected through serpentine flow channels to construct coupled high-throughput microtissue models. Alternatively, independent rows of chambers can be arranged for different microtissue constructs, enabling communication between multiple organoids through the top flow channels. Furthermore, the multilayered configuration allows the integration of a functional sensing layer that enables noninvasive, continuous monitoring of both mechanobiological responses and metabolic processes during dynamic culture conditions. We demonstrated one of these applications for high-throughput drug testing. For the top layer, the channels can be designed using functional microfluidic devices, such as a classic Christmas-tree structure, for generating concentration gradients. This arrangement enables different concentration gradients to cover tissue chamber regions. Such a design significantly enhances high-throughput compound testing efficiency.

This study on multilayer microfluidic platforms has several limitations that need further optimization. First, the multilayered design requires precise interlayer alignment and robust bonding to prevent structural failure and fluid leakage. Although chemical bonding strategies have been successfully implemented for integrating the PDMS layers with PET porous membranes [39], standardized fabrication protocols remain to be established. Second, although hydrostatic pressure-driven perfusion enables IF generation for the development of vascular networks, inherent flow instability limits precise fluidic control. Transitioning to programmable pumping systems could improve flow stability. Third, although the current model using HUVECs and tumor cell lines recapitulates the basic TME, it lacks patient-specific pathophysiological relevance. Incorporating patient-derived tumor organoids with immune components can improve personalized therapeutic screening capabilities. Notably, tumor models incorporating functional and perfusable microvascular networks represent an ideal platform for exploring the processes of migration, adhesion, infiltration, and target cytotoxicity of immune cells. Recent advancements in circulatory-perfused vascularized tumor models have enabled the recapitulation of tissue-specific macrophage infiltration dynamics and monocyte differentiation processes [62]. In particular, the OOC technology has emerged as a promising tool for the systematic investigation of combinatorial cancer immunotherapies. A seminal study using a microvascularized tumor-on-a-chip platform quantitatively demonstrated TME-mediated immunosuppression of natural killer (NK) cells and simultaneously established that coadministration of immune checkpoint inhibitors effectively reverses the exhaustion of NK cells [63]. Another study used a perfusable vascularized tumor model and clarified the mechanistic insights into T-cell transport patterns across the vascular network [64]. The analysis revealed that PD-1 checkpoint blockade significantly improves the activation status of T cells, resulting in a marked improvement in the killing efficiency of tumor cells.

## 5 Conclusions

The multilayered microfluidic platform described in our study addresses a critical challenge in the construction of 3D vascularized OOC models. By incorporating a porous membrane as a hydrogel-patterned barrier, the platform ensures stable and precise hydrogel loading, effectively preventing leakage and facilitating efficient nutrient and oxygen exchange. This design not only improves the robustness of the system but also facilitates the formation of complex vascular networks that closely resemble in vivo conditions. The platform successfully recapitulates key vascular processes, including angiogenesis, vasculogenesis, and tumor vascular formation, representing a versatile tool for exploring vascular mechanisms and the TME. Moreover, the multilayered platform provides exceptional flexibility and scalability, making it ideal for high-throughput drug screening and multiorgan interconnected systems. Validation through antitumor drug efficacy evaluations highlights its potential as a preclinical in vitro model for cancer research and drug development. In conclusion, this platform provides significant versatility for vascularizing diverse microtissues and holds promise as a high-throughput platform for multiorgan integration with relevance for preclinical drug screening.

**Supplementary Information** The online version contains supplementary material available at https://doi.org/10.1631/bdm.2500091.

**Acknowledgements** This work was supported by grants from the Interdisciplinary Program of Shanghai Jiao Tong University (No. YG2023LC04), the National Natural Science Foundation of China (Nos. 32471473, 62231025, and 82171011), the Research Program of Shanghai Science and Technology Committee (Nos. 24141900900 and 25JC3201100), and Chongqing Natural Science Foundation (No. CSTB2022NSCQ-MSX0767). The authors were also grateful to the Center for Advanced Electronic Materials and Devices (AEMD) of Shanghai Jiao Tong University.

**Author contributions** CYZ and XLW designed the microfluidic platform. CYZ and ZJL were involved in fabricating the platform. JQX was involved in culturing cells. CYZ was involved in constructing the models on the platform. CYZ, DYY, and LX were involved in statistical analysis. CYZ, ZJL, and JQX were involved in drafting the manuscript. XLW conceived and administered the research. All the authors have read, revised, and commented on the manuscript prior to submission.

## Declarations

**Conflict of interest** The authors declare that they have no conflict of interest.

**Ethical approval** This article does not contain any studies with human or animal subjects performed by any of the authors.

**Data availability** The data that support the findings of this study are available from the corresponding author upon reasonable request.

## References

1. Mao AS, Mooney DJ (2015) Regenerative medicine: current therapies and future directions. Proc Natl Acad Sci USA 112(47): 14452–14459. https://doi.org/10.1073/pnas.1508520112
2. Sbierski-Kind J, Mroz N, Molofsky AB (2021) Perivascular stromal cells: directors of tissue immune niches. Immunol Rev 302(1):10–31. https://doi.org/10.1111/imr.12984
3. Liu ZL, Chen HH, Zheng LL et al (2023) Angiogenic signaling pathways and anti-angiogenic therapy for cancer. Signal Transduct Target Ther 8(1):198. https://doi.org/10.1038/s41392-023-01460-1
4. Lopes-Coelho F, Martins F, Pereira SA et al (2021) Anti-angiogenic therapy: current challenges and future perspectives. Int J Mol Sci 22(7):3765. https://doi.org/10.3390/ijms22073765
5. Hurwitz H, Fehrenbacher L, Novotny W et al (2004) Bevacizumab plus irinotecan, fluorouracil, and leucovorin for metastatic colorectal cancer. N Engl J Med 350(23):2335–2342. https://doi.org/10.1056/NEJMoa032691
6. Mokhtari RB, Homayouni TS, Baluch N et al (2017) Combination therapy in combating cancer. Oncotarget 8(23):38022–38043. https://doi.org/10.18632/oncotarget.16723
7. Jiang W, Guo ZX, Wang Q et al (2025) Enhanced nanoparticle delivery across vascular basement membranes of tumours using nitric oxide. Nat Biomed Eng 9:1486–1501. https://doi.org/10.1038/s41551-025-01385-w
8. Tylawsky DE, Kiguchi H, Vaynshteyn J et al (2023) P-selectin-targeted nanocarriers induce active crossing of the blood–brain barrier via caveolin-1-dependent transcytosis. Nat Mater 22(3): 391–399. https://doi.org/10.1038/s41563-023-01481-9
9. Omidian H, Babanejad N, Cubeddu LX (2023) Nanosystems in cardiovascular medicine: advancements, applications, and future perspectives. Pharmaceutics 15(7):1935. https://doi.org/10.3390/pharmaceutics15071935
10. Low LA, Mummery C, Berridge BR et al (2021) Organs-on-chips: into the next decade. Nat Rev Drug Discov 20(5):345–361. https://doi.org/10.1038/s41573-020-0079-3
11. Ingber DE (2022) Human organs-on-chips for disease modelling, drug development and personalized medicine. Nat Rev Genet 23(8):467–491. https://doi.org/10.1038/s41576-022-00466-9
12. Gong XF, Yang C, Peng JC et al (2025) Vascularized organoid-on-a-chip for centimeter-scale organoid cultivation. Bio-Des Manuf 8(3):410–422. https://doi.org/10.1631/bdm.2400424
13. Tavakol DN, Nash TR, Kim Y et al (2024) Modeling the effects of protracted cosmic radiation in a human organ-on-chip platform. Adv Sci 11(42):e2401415. https://doi.org/10.1002/advs.202401415
14. Vo Q, Carlson KA, Chiknas PM et al (2024) On-chip reconstitution of uniformly shear-sensing 3D matrix-embedded multicellular blood microvessel. Adv Funct Mater 34(10):2304630. https://doi.org/10.1002/adfm.202304630
15. Whitworth CP, Polacheck WJ (2024) Vascular organs-on-chip made with patient-derived endothelial cells: technologies to transform drug discovery and disease modeling. Expert Opin Drug Discov 19(3):339–351. https://doi.org/10.1080/17460441.2023.2294947
16. de Haan L, Suijker J, van Roey R et al (2021) A microfluidic 3D endothelium-on-a-chip model to study transendothelial

migration of T cells in health and disease. Int J Mol Sci 22(15): 8234.
https://doi.org/10.3390/ijms22158234
17. Thacker VV, Sharma K, Dhar N et al (2021) Rapid endotheliitis and vascular damage characterize SARS-CoV-2 infection in a human lung-on-chip model. EMBO Rep 22(6):e52744.
https://doi.org/10.15252/embr.202152744
18. Wang D, Li QY, Zhou CY et al (2024) Dissolvable temporary barrier: a novel paradigm for flexible hydrogel patterning in organ-on-a-chip models. Bio-Des Manuf 7(2):153–166.
https://doi.org/10.1007/s42242-023-00267-x
19. Pavesi A, Tan AT, Koh S et al (2017) A 3D microfluidic model for preclinical evaluation of TCR-engineered T cells against solid tumors. JCI Insight 2(12):e89762.
https://doi.org/10.1172/jci.insight.89762
20. Chuaychob S, Lyu RY, Tanaka M et al (2024) Mimicking angiogenic microenvironment of alveolar soft-part sarcoma in a microfluidic coculture vasculature chip. Proc Natl Acad Sci USA 121(13):e2312472121.
https://doi.org/10.1073/pnas.2312472121
21. Jeon JS, Bersini S, Gilardi M et al (2015) Human 3D vascularized organotypic microfluidic assays to study breast cancer cell extravasation. Proc Natl Acad Sci USA 112(1):214–219.
https://doi.org/10.1073/pnas.1417115112
22. Ahn J, Lim J, Jusoh N et al (2019) 3D microfluidic bone tumor microenvironment comprised of hydroxyapatite/fibrin composite. Front Bioeng Biotechnol 7:168.
https://doi.org/10.3389/fbioe.2019.00168
23. Ko EC, Spitz S, Pramotton FM et al (2023) Accelerating the in vitro emulation of Alzheimer's disease-associated phenotypes using a novel 3D blood-brain barrier neurosphere co-culture model. Front Bioeng Biotechnol 11:1251195.
https://doi.org/10.3389/fbioe.2023.1251195
24. Pavlou G, Spitz S, Pramotton FM et al (2025) Engineered 3D human neurovascular model of Alzheimer's disease to study vascular dysfunction. Biomaterials 314:122864.
https://doi.org/10.1016/j.biomaterials.2024.122864
25. Arslan U, Brescia M, Meraviglia V et al (2023) Vascularized hiPSC-derived 3D cardiac microtissue on chip. Stem Cell Reports 18(10):2003.
https://doi.org/10.1016/j.stemcr.2023.08.012
26. Au AK, Lai H, Utela BR et al (2011) Microvalves and micropumps for BioMEMS. Micromachines 2(2):179–220.
https://doi.org/10.3390/mi2020179
27. Wang XL, Phan DTT, Sobrino A et al (2016) Engineering anastomosis between living capillary networks and endothelial cell-lined microfluidic channels. Lab Chip 16(2):282–290.
https://doi.org/10.1039/C5LC01050K
28. Phan DTT, Wang XL, Craver BM et al (2017) A vascularized and perfused organ-on-a-chip platform for large-scale drug screening applications. Lab Chip 17(3):511–520.
https://doi.org/10.1039/C6LC01422D
29. Cuenca MV, Cochrane A, van den Hil FE et al (2021) Engineered 3D vessel-on-chip using hiPSC-derived endothelial- and vascular smooth muscle cells. Stem Cell Rep 16(9):2159–2168.
https://doi.org/10.1016/j.stemcr.2021.08.003
30. Trietsch SJ, Israëls GD, Joore J et al (2013) Microfluidic titer plate for stratified 3D cell culture. Lab Chip 13(18):3548–3554.
https://doi.org/10.1039/C3LC50210D
31. Park JY, Mani S, Clair G et al (2022) A microphysiological model of human trophoblast invasion during implantation. Nat Commun 13(1):1252.
https://doi.org/10.1038/s41467-022-28663-4
32. Wang XL, Phan DTT, Zhao D et al (2016) An on-chip microfluidic pressure regulator that facilitates reproducible loading of cells and hydrogels into microphysiological system platforms. Lab Chip 16(5):868–876.
https://doi.org/10.1039/C5LC01563D
33. Lee J, Jung S, Hong HK et al (2024) Vascularized tissue on mesh-assisted platform (VT-MAP): a novel approach for diverse organoid size culture and tailored cancer drug response analysis. Lab Chip 24(8):2208–2223.
https://doi.org/10.1039/d3lc01055d
34. Ko J, Ahn J, Kim S et al (2019) Tumor spheroid-on-a-chip: a standardized microfluidic culture platform for investigating tumor angiogenesis. Lab Chip 19(17):2822–2833.
https://doi.org/10.1039/C9LC00140A
35. Yu J, Lee S, Song J et al (2022) Perfusable micro-vascularized 3D tissue array for high-throughput vascular phenotypic screening. Nano Converg 9(1):16.
https://doi.org/10.1186/s40580-022-00306-w
36. Lee SR, Kim Y, Kim S et al (2022) U-IMPACT: a universal 3D microfluidic cell culture platform. Microsyst Nanoeng 8:126.
https://doi.org/10.1038/s41378-022-00431-w
37. Lai XC, Yang MP, Wu H et al (2022) Modular microfluidics: current status and future prospects. Micromachines 13(8):1363.
https://doi.org/10.3390/mi13081363
38. Yue T, Zhao D, Phan DTT et al (2021) A modular microfluidic system based on a multilayered configuration to generate large-scale perfusable microvascular networks. Microsyst Nanoeng 7:4.
https://doi.org/10.1038/s41378-020-00229-8
39. Wu WM, Wu J, Kim JH et al (2015) Instantaneous room temperature bonding of a wide range of non-silicon substrates with poly(dimethylsiloxane) (PDMS) elastomer mediated by a mercaptosilane. Lab Chip 15(13):2819–2825.
https://doi.org/10.1039/C5LC00285K
40. Hsu YH, Moya ML, Abiri P et al (2013) Full range physiological mass transport control in 3D tissue cultures. Lab Chip 13(1): 81–89.
https://doi.org/10.1039/C2LC40787F
41. Kim S, Chung M, Ahn J et al (2016) Interstitial flow regulates the angiogenic response and phenotype of endothelial cells in a 3D culture model. Lab Chip 16(21):4189–4199.
https://doi.org/10.1039/c6lc00910g
42. Tan SY, Jing QY, Leung Z et al (2022) Transcriptomic analysis of 3D vasculature-on-a-chip reveals paracrine factors affecting vasculature growth and maturation. Lab Chip 22(20):3885–3897.
https://doi.org/10.1039/D2LC00570K
43. Shams F, Moravvej H, Hosseinzadeh S et al (2022) Overexpression of VEGF in dermal fibroblast cells accelerates the angiogenesis and wound healing function: in vitro and in vivo studies. Sci Rep 12(1):18529.
https://doi.org/10.1038/s41598-022-23304-8
44. Zhao YJ, Adjei AA (2015) Targeting angiogenesis in cancer therapy: moving beyond vascular endothelial growth factor. Oncologist 20(6):660–673.
https://doi.org/10.1634/theoncologist.2014-0465
45. Wei XX, Chen YH, Jiang XJ et al (2021) Mechanisms of vasculogenic mimicry in hypoxic tumor microenvironments. Mol Cancer 20(1):7.
https://doi.org/10.1186/s12943-020-01288-1
46. de Visser KE, Joyce JA (2023) The evolving tumor microenvironment: from cancer initiation to metastatic outgrowth. Cancer Cell 41(3):374–403.
https://doi.org/10.1016/j.ccell.2023.02.016
47. Konopka J, Żuchowska A, Jastrzębska E (2024) Vascularized tumor-on-chip microplatforms for the studies of neovasculature as hope for more effective cancer treatments. Biosens Bioelectron

249:115986.
https://doi.org/10.1016/j.bios.2023.115986
48. Zhou CY, Li ZJ, Lu KY et al (2025) Advances in human organs-on-chips and applications for drug screening and personalized medicine. Fundam Res 5(3):1258–1272.
https://doi.org/10.1016/j.fmre.2023.12.019
49. Zhang ML, Zhang B (2025) Extracellular matrix stiffness: mechanisms in tumor progression and therapeutic potential in cancer. Exp Hematol Oncol 14(1):54.
https://doi.org/10.1186/s40164-025-00647-2
50. Iyer R, Fetterly G, Lugade A et al (2010) Sorafenib: a clinical and pharmacologic review. Expert Opin Pharmacother 11(11): 1943–1955.
https://doi.org/10.1517/14656566.2010.496453
51. Zhang S, Wan ZP, Pavlou G et al (2022) Interstitial flow promotes the formation of functional microvascular networks in vitro through upregulation of matrix metalloproteinase-2. Adv Funct Mater 32(43):2206767.
https://doi.org/10.1002/adfm.202206767
52. Jones S, Bischof H, Lang I et al (2015) Dysregulated flow-mediated vasodilatation in the human placenta in fetal growth restriction. J Physiol 593(14):3077–3092.
https://doi.org/10.1113/JP270495
53. Melincovici CS, Boşca AB, Şuşman S et al (2018) Vascular endothelial growth factor (VEGF) - key factor in normal and pathological angiogenesis. Rom J Morphol Embryol 59(2):455–467
54. Wang WY, Kent RN, Huang SA et al (2021) Direct comparison of angiogenesis in natural and synthetic biomaterials reveals that matrix porosity regulates endothelial cell invasion speed and sprout diameter. Acta Biomater 135:260–273.
https://doi.org/10.1016/j.actbio.2021.08.038
55. Wang WY, Jarman EH, Lin D et al (2021) Dynamic endothelial stalk cell–matrix interactions regulate angiogenic sprout diameter. Front Bioeng Biotechnol 9:620128.
https://doi.org/10.3389/fbioe.2021.620128
56. Bordeleau F, Mason BN, Lollis EM et al (2017) Matrix stiffening promotes a tumor vasculature phenotype. Proc Natl Acad Sci USA 114(3):492–497.
https://doi.org/10.1073/pnas.1613855114
57. Gkretsi V, Stylianopoulos T (2018) Cell adhesion and matrix stiffness: coordinating cancer cell invasion and metastasis. Front Oncol 8:145.
https://doi.org/10.3389/fonc.2018.00145
58. Schrader J, Gordon-Walker TT, Aucott RL et al (2011) Matrix stiffness modulates proliferation, chemotherapeutic response, and dormancy in hepatocellular carcinoma cells. Hepatology 53(4): 1192–1205.
https://doi.org/10.1002/hep.24108
59. Jung HY, Fattet L, Yang J (2015) Molecular pathways: linking tumor microenvironment to epithelial-mesenchymal transition in metastasis. Clin Cancer Res 21(5):962–968.
https://doi.org/10.1158/1078-0432.CCR-13-3173
60. Le MN, Xu KL, Wang Z et al (2021) Evaluation of the effect of 3D porous chitosan-alginate scaffold stiffness on breast cancer proliferation and migration. J Biomed Mater Res Part A 109(10): 1990–2000.
https://doi.org/10.1002/jbm.a.37191
61. Reales-Calderon JA, Lam MSY, Ow JR et al (2022) Microphysiological vascularized solid tumor model for drugs and cell therapies screening. Research Square.
https://doi.org/10.21203/rs.3.rs-1853599/v1
62. Zhang F, Jozani KA, Chakravarty A et al (2025) Immune-infiltrated cancer spheroid model with vascular recirculation reveals temporally dependent and tissue-specific macrophage recruitment. Adv Healthc Mater 14(9):2402946.
https://doi.org/10.1002/adhm.202402946
63. Ayuso JM, Rehman S, Virumbrales-Munoz M et al (2021) Microfluidic tumor-on-a-chip model to evaluate the role of tumor environmental stress on NK cell exhaustion. Sci Adv 7(8): eabc2331.
https://doi.org/10.1126/sciadv.abc2331
64. Zhao YW, Wu Y, Islam K et al (2024) Microphysiologically engineered vessel-tumor model to investigate vascular transport dynamics of immune cells. ACS Appl Mater Interfaces 16(18): 22839–22849.
https://doi.org/10.1021/acsami.4c00391